

Measuring the optical characteristics of medulloblastoma with optical coherence tomography

Barry Vuong,^{1,2,11} Patryk Skowron,^{1,3,11} Tim-Rasmus Kiehl,^{4,5}
 Matthew Kyan,² Livia Garzia,^{3,6,7} Cuiru Sun,¹ Michael D. Taylor,^{2,6,7,8}
 and Victor X.D. Yang^{1,8,9,10,*}

¹ Biophotonics and Bioengineering Laboratory, Ryerson University, 350 Victoria Street, Toronto, ON, M5B 2K3, Canada

² Department of Electrical and Computer Engineering, Ryerson University, 350 Victoria St., Toronto, M4B 2K3, Canada

³ Hospital for Sick Children, Arthur and Sonia Labatt Brain Tumour Research Centre and Division of Neurosurgery, 686 Bay Street, Toronto, M5G 1L7, Canada

⁴ University Health Network, Department of Pathology, 190 Elizabeth St., Toronto, M5G 2C4, Canada

⁵ University of Toronto, Department of Laboratory Medicine and Pathobiology, 172 St George St, Toronto, M5R 0A3, Canada

⁶ Hospital for Sick Children, Program in Developmental and Stem Cell Biology, 555 University Avenue, Toronto, M5G 1X8, Canada

⁷ University of Toronto, Department of Laboratory Medicine and Pathobiology, 1 King's College Circle, Toronto, M5S 1A8, Canada

⁸ Division of Neurosurgery, Faculty of Medicine, University of Toronto, 1 King's College Circle, Toronto, ON, M5S 1A8, Canada

⁹ Physical Science - Brain Sciences Research Program, Sunnybrook Research Institute, 2075 Bayview Avenue, Toronto, ON, M4N 3M5, Canada

¹⁰ Division of Neurosurgery, Sunnybrook Health Sciences Centre, 2075 Bayview Avenue, Toronto, ON, M4N 3M5, Canada

¹¹ These authors contributed equally to this work

*yangv@ee.ryerson.ca

Abstract: Medulloblastoma is the most common malignant pediatric brain tumor. Standard treatment consists of surgical resection, followed by radiation and high-dose chemotherapy. Despite these efforts, recurrence is common, leading to reduced patient survival. Even with successful treatment, there are often severe long-term neurologic impacts on the developing nervous system. We present two quantitative techniques that use a high-resolution optical imaging modality: optical coherence tomography (OCT) to measure refractive index, and the optical attenuation coefficient. To the best of our knowledge, this study is the first to demonstrate OCT analysis of medulloblastoma. Refractive index and optical attenuation coefficient were able to differentiate between normal brain tissue and medulloblastoma in mouse models. More specifically, optical attenuation coefficient imaging of normal cerebellum displayed layers of grey matter and white matter, which were indistinguishable in the structural OCT image. The morphology of the tumor was distinct in the optical attenuation coefficient imaging. These inherent properties may be useful during neurosurgical intervention to better delineate tumor boundaries and minimize resection of normal tissue.

© 2015 Optical Society of America

OCIS codes: (110.4500) Optical coherence tomography; (170.6935) Tissue characterization; (100.2960) Image analysis; (290.1350) Backscattering.

References and links

1. R. J. Gilbertson, "Medulloblastoma: signalling a change in treatment," *The Lancet Oncology* **5**, 209–218 (2004).
2. J. M. Legler, L. A. G. Ries, M. A. Smith, J. L. Warren, E. F. Heineman, R. S. Kaplan, and M. S. Linet, "Brain and other central nervous system cancers: recent trends in incidence and mortality," *J. Nat. Cancer Inst.* **91**, 1382–1390 (1999).
3. A. Gajjar, R. Hernan, M. Kocak, C. Fuller, Y. Lee, P. J. McKinnon, D. Wallace, C. Lau, M. Chintagumpala, D. M. Ashley, S. J. Kellie, L. Kun and R. J. Gilbertson, "Clinical, histopathologic, and molecular markers of prognosis: toward a new disease risk stratification system for medulloblastoma," *J. Clin. Oncol.* **22**, 984–993 (2004).
4. V. Kumar, A. K. Abbas, N. Fausto, and J. C. Aster, *Robbins and Cotran Pathologic Basis of Disease, Professional Edition: Expert Consult-Online*, 8th ed. (Elsevier Health Sciences, 2009).
5. C.-H. Pui, A. J. Gajjar, J. R. Kane, I. A. Qaddoumi, and A. S. Pappo, "Challenging issues in pediatric oncology," *Nat. Rev. Clin. Oncol.* **8**, 540–549 (2011).
6. M. Dennis, B. J. Spiegler, C. R. Hetherington, and M. L. Greenberg, "Neuropsychological sequelae of the treatment of children with medulloblastoma," *J. Neuro-Oncol.* **29**, 91–101 (1996).
7. T. Gudrunardottir, B. Lannering, M. Remke, M. D. Taylor, E. M. Wells, R. F. Keating, and R. J. Packer, "Treatment developments and the unfolding of the quality of life discussion in childhood medulloblastoma: a review," *Child's Nervous System* **1**, 1–12 (2014).
8. T. S. Park, H. J. Hoffman, E. B. Hendrick, R. P. Humphreys, and L. E. Becker, "Medulloblastoma: Clinical presentation and management: Experience at the hospital for sick children, toronto, 1950–1980," *J. Neurosurg.* **58**, 543–552 (1983).
9. P. A. Northcott, D. T. Jones, M. Kool, G. W. Robinson, R. J. Gilbertson, Y.-J. Cho, S. L. Pomeroy, A. Korshunov, P. Lichter, M. D. Taylor, and S. M. Pfister, "Medulloblastomics: the end of the beginning," *Nat. Rev. Cancer* **12**, 818–834 (2012).
10. O. Assayag, K. Grieve, B. Devaux, F. Harms, J. Pallud, F. Chretien, C. Boccara, and P. Varlet, "Imaging of non-tumorous and tumorous human brain tissues with full-field optical coherence tomography," *NeuroImage: Clinical* **2**, 549–557 (2013).
11. H. Böhringer, D. Boller, J. Leppert, U. Knopp, E. Lankenau, E. Reusche, G. Hüttmann, and A. Giese, "Time-domain and spectral-domain optical coherence tomography in the analysis of brain tumor tissue," *Lasers Surg. Med.* **38**, 588–597 (2006).
12. H. Böhringer, E. Lankenau, F. Stellmacher, E. Reusche, G. Hüttmann, and A. Giese, "Imaging of human brain tumor tissue by near-infrared laser coherence tomography," *Acta Neurochir.* **151**, 507–517 (2009).
13. S. W. Jeon, M. A. Shure, K. B. Baker, D. Huang, A. M. Rollins, A. Chahalvi, and A. R. Rezai, "A feasibility study of optical coherence tomography for guiding deep brain probes," *J. Neurosci. Methods* **154**, 96–101 (2006).
14. I. V. Turchin, R. Richards-Kortum, E. A. Sergeeva, L. S. Dolin, V. A. Kamensky, and N. M. Shakhova, "Novel algorithm of processing optical coherence tomography images for differentiation of biological tissue pathologies," *J. Biomed. Opt.* **10**, 064024 (2005).
15. K. Barwari, D. M. de Bruin, E. C. Cauberg, D. J. Faber, T. G. van Leeuwen, H. Wijkstra, J. de la Rosette, and M. P. Laguna, "Advanced diagnostics in renal mass using optical coherence tomography: a preliminary report," *J. Endourol.* **25**, 311–315 (2011).
16. F. J. van der Meer, D. J. Faber, D. B. Sassoon, M. C. Aalders, G. Pasterkamp, and T. G. van Leeuwen, "Localized measurement of optical attenuation coefficients of atherosclerotic plaque constituents by quantitative optical coherence tomography," *IEEE Trans. Med. Imaging* **24**, 1369–1376 (2005).
17. G. Van Soest, S. Koljenović, B. E. Bouma, G. J. Tearney, J. W. Oosterhuis, P. W. Serruya, A. F. van der Steen, N. Gonzalo, S. van Noorden, G. L. van Leenders *et al.*, "Atherosclerotic tissue characterization in vivo by optical coherence tomography attenuation imaging," *J. Biomed. Opt.* **15**, 011105 (2010).
18. C. Xu, S. G. Carlier, R. Virmani, and J. M. Schmitt, "Characterization of atherosclerosis plaques by measuring both backscattering and attenuation coefficients in optical coherence tomography," *J. Biomed. Opt.* **13**, 034003 (2008).
19. G. van Soest, M. Villiger, E. Regar, G. J. Tearney, B. E. Bouma, and A. F. van der Steen, "Frequency domain multiplexing for speckle reduction in optical coherence tomography," *J. Biomed. Opt.* **17**, 0760181 (2012).
20. L. Scolaro, R. A. McLaughlin, B. R. Klyen, B. A. Wood, P. D. Robbins, C. M. Saunders, S. L. Jacques, and D. D. Sampson, "Parametric imaging of the local attenuation coefficient in human axillary lymph nodes assessed using optical coherence tomography," *Biomed. Opt. Express* **3**, 366–379 (2012).
21. B. R. Klyen, L. Scolaro, T. Shavlakadze, M. D. Grounds, and D. D. Sampson, "Optical coherence tomography can assess skeletal muscle tissue from mouse models of muscular dystrophy by parametric imaging of the attenuation coefficient," *Biomed. Opt. Express* **5**, 1217–1232 (2014).
22. P. Gong, R. A. McLaughlin, Y. M. Liew, P. R. Munro, F. M. Wood, and D. D. Sampson, "Assessment of human burn scars with optical coherence tomography by imaging the attenuation coefficient of tissue after vascular masking," *J. Biomed. Opt.* **19**, 021111 (2014).

23. C. P. Fleming, J. Eckert, E. F. Halpern, J. A. Gardecki, and G. J. Tearney, "Depth resolved detection of lipid using spectroscopic optical coherence tomography," *Biomed. Opt. Express* **4**, 1269–1284 (2013).
24. J. Sun, S. J. Lee, L. Wu, M. Sarntinoranont, and H. Xie, "Refractive index measurement of acute rat brain tissue slices using optical coherence tomography," *Opt. Express* **20**, 1084–1095 (2012).
25. G. Tearney, M. Brezinski, B. Bouma, M. Hee, J. Southern, and J. Fujimoto, "Determination of the refractive index of highly scattering human tissue by optical coherence tomography," *Opt. Lett.* **20**, 2258–2260 (1995).
26. X. Wu, P. A. Northcott, A. Dubuc, A. J. Dupuy, D. J. Shih, H. Witt, S. Croul, E. Bouffet, D. W. Fults, C. G. Eberhart, J. Majewski, T. E. Scheetz, S. M. Pfister, A. Korshunov, X. Li, S. W. Scherer, Y. Cho, K. Akagi, T. J. MacDonald, J. Koster, M. G. McCabe, A. L. Sarver, P. Collins, W. A. Weiss, D. A. Largaespada, L. S. Collier, and M. D. Taylor, "Clonal selection drives genetic divergence of metastatic medulloblastoma," *Nature (London)* **482**, 529–533 (2012).
27. A. M. Dubuc, P. A. Northcott, A. M. Kenney, and M. D. Taylor, "Calculating a cure for cancer: managing medulloblastoma mathematically," *Expert Rev. Neurother.* **10**, 1489–1492 (2010).
28. C. Sun, B. Standish, B. Vuong, X.-Y. Wen, and V. X.D. Yang, "Digital image correlation-based optical coherence elastography," *J. Biomed. Opt.* **18**, 121515 (2013).
29. D. Comaniciu and P. Meer, "Mean shift: A robust approach toward feature space analysis," *IEEE Trans. Pattern Analysis and Machine Intelligence* **24**, 603–619 (2002).
30. W. Tao, H. Jin, and Y. Zhang, "Color image segmentation based on mean shift and normalized cuts," *IEEE Trans. Systems, Man, and Cybernetics, Part B: Cybernetics*, **37**, 1382–1389 (2007).
31. S. W. Jeon, M. A. Shure, K. B. Baker, D. Huang, A. M. Rollins, A. Chahalvi, and A. R. Rezai, "A feasibility study of optical coherence tomography for guiding deep brain probes," *J. Neurosci. Meth.* **154**, 96–10 (2006).
32. F. Bevilacqua, D. Piguet, P. Marquet, J. D. Gross, B. J. Tromberg, and C. Depeursinge, "In vivo local determination of tissue optical properties: applications to human brain," *Appl. Opt.* **38**, 4939–4950 (1999).

1. Introduction

Brain tumors are the second most common pediatric cancer (after leukaemia) in the United States [1]. It is estimated that more than 3 per 100,000 children per year are affected by brain tumors in the United States [2]. Among pediatric brain tumors, medulloblastoma is the most prominent malignant tumor with the greatest tendency to metastasize [3]. Proliferation of this tumor often occludes the flow of cerebrospinal fluid resulting in hydrocephalus [4]. Overall, medulloblastoma is the leading cause of cancer-related mortality in children [5]. Current standard of care consists of surgical resection, chemotherapy, and high-dose radiation. Radiation is often an effective treatment for medulloblastoma, but nearly 90% of pediatric patients have impaired intelligence and many develop subsequent neurocognitive dysfunction [6]. As a result, careful treatment planning is critical and its success is directly linked to the child's quality of life [7]. In the initial treatment, emphasis has been placed on surgical resection and chemotherapy. The completeness of surgical resection is statistically correlated to the prognosis of the child [8]. Patients with more than 1.5 cm^2 of enhancing residual tumor on MRI after surgery are classified as high risk [9]. The problem confronting the neurosurgeon is that there may be minimal inherent optical contrast between normal brain tissue and tumor tissue during surgery. This could lead to surgical margins that may not be adequately identified, possibly increasing the risk of recurrence.

Recent developments in optical coherence tomography (OCT) have resulted in an emerging biomedical imaging modality for the evaluation of brain tumors, providing microstructural resolution and correlation with histology for interpretation [10]. Although OCT provides high-resolution images, it still relies on a trained reader to interpret the information. Previous studies have employed classification schemes to assist and quantify measurements from OCT images based on optical attenuation coefficient, μ_t , and refractive index. In terms of optical attenuation coefficient, *ex vivo* and *in vivo* images of human glioma specimens were acquired and the mean optical attenuation coefficient was measured [11–13]. This consisted of the evaluation of an area of interest within a single frame [14, 15]. The local attenuation can provide the ability to construct an optical coherence tomography optical attenuation (OCT-OA) image [16–23]. These images have also shown good correlation with histology and provide additional contrast

over the structural OCT image. An alternative and simple quantitative method for measuring the optical properties of tissue using OCT is refractive index. This was shown to be very accurate in identifying various anatomical tissues such as brain [24], skin, adipose tissue, and muscle [25].

In this study, we present quantitative measurements of optical attenuation coefficient and refractive index using optical coherence tomography in endogenous mouse models of medulloblastoma. To the best of our knowledge, refractive index measurement, structural OCT images, and the corresponding optical attenuation images of medulloblastoma have not been previously presented. Comparison of both normal cerebellum and infiltrated medulloblastoma tissue were acquired and ranges of values were reported. Verification of these measurements was then correlated with histology.

2. Materials and methods

2.1. Mouse model

Patched 1 (*Ptch*^{+/−}) mouse models harbor a mutation in one allele of the *Ptch* gene. They have a penetrance of 30% and develop tumors by 8 months of age [26]. *Math1-GFP;Ptch*^{+/−} contained the heterozygous *Ptch* mutation as well as a green fluorescent protein (GFP) reporter downstream of *Math1*, a cerebellar progenitor cell specific promoter [27]. After the development of the mouse cerebellum, the expression of the GFP reporter is restricted to medulloblastoma tumor tissue. Normal mouse models were also collected to serve as a control. The mouse protocol was approved by the Animal Care Committee at The Toronto Centre for Phenogenomics (Toronto, Canada).

2.2. Phantom model

A 1 mm outer diameter silicone tube was incased in a titanium dioxide (0.5 g/l) versa gel phantom. A diluted concentration of intralipid (0.5% with distilled water) was injected within the lumen of the silicone tube and was stationary during imaging. This phantom was a simplified model of the cortical region of the brain and was used to evaluation the optical attenuation technique.

2.3. Imaging Protocol

Entire mouse brains (*Ptch*^{+/−} = 6 and Normal = 4) were harvested and kept on ice in artificial cerebrospinal fluid (ACSF) (132mM *NaCl*, 3.0mM *KCl*, 1.25mM *NaH₂PO₄*, 2mM *MgCl₂*, 11mM D-glucose, 20mM *NaHCO₃*, 2mM *CaCl₂*, saturated with 95% *O₂* (balance 5% *CO₂*), pH = 7.4, 315–325 Osm) during downstream analysis. *Math1-GFP;Ptch*^{+/−} brains were imaged with an Olympus SZX16 microscope. Fluorescent images of *Ptch*^{+/−} were taken during excitation with a 395 nm laser and overlapped with the bright-field images in ImageJ 10.2 (NIH, USA). The superimposed images were used as a reference during OCT imaging. Samples were imaged in ACSF using an in-house built polygon based swept source laser [28], which had a center wavelength of 1310 nm, a full width half maximum bandwidth of 110 nm (axial resolution ≈ 7 μm in air), and an output power of ≈ 30 mW at an A-line frequency of 36 kHz. The majority of the output swept source laser power (90%) was tapped to the MZI clock for k-space resampling, while 10% was used for a Fiber Bragg Grating (FBG) to trigger the data acquisition card. After the MZI clock, the remaining power (80% of the swept source laser) was coupled to a fiber-based interferometer, where the light was reflected back from a reference mirror and sample arm (lateral resolution ≈ 20 μm). These were then combined and detected using a balanced photodetector (PDB-440 Thorlabs, USA). Two-dimensional images were digitally sectioned in OsiriX (V4.1.2, Switzerland) in order to match the histology. Three-dimensional

images were rendered using ImageJ.

2.4. Optical coherence tomography optical attenuation imaging

As previously demonstrated [17], the basis of the OCT-OA imaging algorithm consisted of the modelling of the optics in the sample arm and the depth roll-off of the swept source laser. This study assumed that only single scattering events were measured. Therefore, the measured OCT signal can be approximated by a Beer-Lambert exponential decay, [17]

$$\langle I_d(z) \rangle = I_o T(z) S(z) \exp[-\mu_t z], \quad (1)$$

where the measured OCT signals, $I_d(z)$, is averaged over several realizations, denoted by $\langle \rangle$. Averaging improved the signal-to-noise ratio and removed speckle generated by the tissue. I_o is the locally available intensity, which is equal to the initial value of the reflectance at the tissue surface and μ_t is the optical attenuation coefficient. The longitudinal point spread function of the OCT system is denoted as $T(z)$ and is characterized by [17]

$$T(z) = \left[\left(\frac{z - z_o}{z_R} \right)^2 + 1 \right]^{-\frac{1}{2}}, \quad (2)$$

where the Rayleigh length is defined as $z_R = 5\text{mm}$ and the position of the beam waist $z_o = 19.4\text{mm}$. In this study, a swept laser source was utilized to acquire the OCT. As a result, the signal roll-off with depth ($S(z)$) must be taken into account [17]

$$S(z) = \exp\left[-\left(\frac{z}{z_w}\right)^2\right], \quad (3)$$

where z_w is the half width of the roll-off function and was measured to be 3 mm. The intensity signal was linearized by logarithmic compression based on the geometric optics of the lens at the sample arm (AC254-030-C-ML, Thorlabs, USA) [17]

$$i_d = \log[\langle I_d(z) \rangle] - \log[T(z)] - \log[S(z)]. \quad (4)$$

At the surface of the tissue (detected through thresholding), Eq. 4 was least squared fitted with a variable minimum window length of the following model [17]

$$i(z) = \log[I_o] - \mu_t z. \quad (5)$$

To extract μ_t , homogeneous tissue regions were isolated by a cost versus fit procedure [17]. The minimum length of the window for this fitting procedure was determined using an image segmentation technique known as mean shift segmentation [29, 30] with an absolute minimum window size of 5 pixels ($\sim 30 \mu\text{m}$). This would provide sufficient sampling as the molecular layer of the cerebellum in mice is greater than $60 \mu\text{m}$. Mean shift segmentation is a robust feature space analysis that consists of an unsupervised clustering based segmentation method. This method operates under conditions where the number and shape of the data cluster is unknown [30]. The general concept behind the mean shift algorithm is that a random data point is initially chosen. Within a set radius of the data point ($r = 4$ pixels, $\sim 23 \mu\text{m}$), the mean of the data points was computed. Next, the center of the radius was shifted to the calculated mean. This process was repeated until the calculated center radius converged. In this study, the averaged B-mode OCT image ($N_{avg} = 4$ frames) was over segmented by the mean shift algorithm to produce a large number of boundaries. The result of mean shift segmentation of a human finger can be seen from Fig. 1(b). Similar intensities are segmented and used as the boundaries between different tissues, which is represented in color in Fig. 1(b). This functioned as a guide

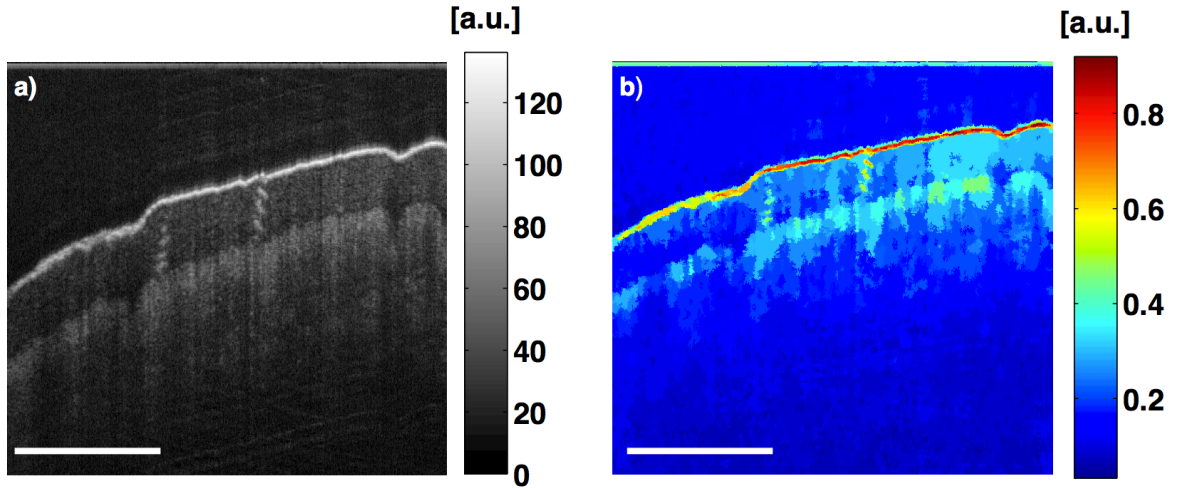


Fig. 1. (a) An OCT image of human fingertips. (b) The result of mean shift segmentation from the OCT image based on clustering. Each color in the mean shift segmentation image represents a segmented area. Scale bar is 1mm.

for an adaptive minimum window length procedure during the iterative optical attenuation coefficient estimation. The window was then increased incrementally and a cost was computed until convergence, as outlined in the original algorithm [17]. Once the attenuation coefficients were calculated, a moving window in the depth direction evaluated the SNR and compared it to the previous position of the window. If the SNR had decreased relative to the previous position of the window, all calculated attenuation coefficients below this position was rejected. This differs from previous OCT-OA imaging, where the minimum window was initially set. Instead, the window size was estimated based on the similarity of intensity values in the surrounding region.

A calibration step was introduced for the OCT-OA images in order to remove the system dependence ($S(z)$ & $T(z)$). Prior to imaging of the cerebellum, a homogeneous phantom (polystyrene microspheres diluted in distilled water) with known optical properties (μ_p and I_{po}) was imaged [20]. As a result, equation 4 & 5 were then modified to the following, in order to account for the optical properties of polystyrene microspheres.

$$i_c = \log[\langle I_d(z) \rangle] - \log[\langle I_p(z) \rangle], \quad (6)$$

$$i(z) = \log\left[\frac{I_o}{I_{po}}\right] - \mu_c z, \quad (7)$$

$$\mu_c = \mu_t - \mu_p, \quad (8)$$

where i_c is the OCT signal, $\langle I_p(z) \rangle$ is the measured OCT signals of the phantom, I_{po} is the locally available intensity, which is equal to the initial value of the reflectance at the phantom surface, μ_c is the optical attenuation coefficient and μ_p is the optical attenuation coefficient of the phantom and was previously calculated to be 0.69 mm^{-1} [20].

2.5. Refractive index measurement

Initial methods for the measurement of refractive index were proposed by Tearney *et al.* [25]. Although two accurate methods were proposed, we employed the method in which the specimen was imaged on a planar reflective surface (a metal plate). Three-dimensional OCT images of normal and tumor sites were acquired. The thickness of the specimen (z) was determined by the difference between the surface of the metal plate and surface of the specimen in the selected ($N_{frame} = 3$) two-dimensional OCT image (Fig. 2(d)). Next, the optical path length delay (z') was obtained by the difference in the surface of the metal plate and the image through the plate (Fig. 2(d)). As a result, the refractive index could be computed by the following [25]

$$n = \frac{z' + z}{z}. \quad (9)$$

3. Results

3.1. Refractive index imaging

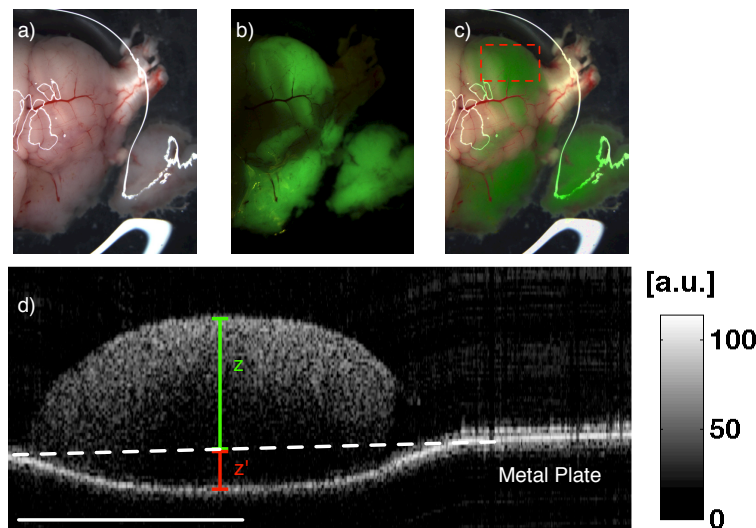


Fig. 2. (a) Gross histology of harvested *Math1-GFP;Ptch⁺⁻* mouse model. (b) The corresponding fluorescence image. (c) The combined gross and fluorescence image. (d) A 500 μm thick section of the fluorescent medulloblastoma (red dashed box) region was imaged by OCT on a planar reflective surface. Refractive index was measured by evaluating the optical thickness of the specimen ($z + z'$). Scale bar is 1 mm.

Both *Math1-GFP;Ptch⁺⁻* and *Ptch⁺⁻* models were utilized during the refractive index measurement. Figure 2 depicts the *Math1-GFP;Ptch⁺⁻* model under a fluorescence microscope. Areas that fluoresce contained medulloblastoma and were sectioned into a thickness of 500 μm using a vibratome (Leica VT1200S). These thin sections of tissue were then imaged by OCT (Fig. 2(d)). A total of 3 medulloblastoma-infiltrated brains were used for the refractive index measurement. Normal cerebellum ($N = 2$) was also sectioned and imaged by OCT. The refractive index measurements were calculated using 10,688 A-lines from the medulloblastoma and 10,571 A-lines from normal. An average of 3 frames per sample were used to evaluate each refractive index. It was observed that the mean refractive indices for normal brain specimens

and medulloblastoma specimens were 1.34 ± 0.038 and 1.36 ± 0.031 , respectively. Similar refractive indices were computed in the *Ptch^{+/−}* models. However, these values did not demonstrate significant difference with the T-test.

3.2. Optical coherence tomography optical attenuation (OCT-OA) imaging

3.2.1. Cortical phantom imaging

The evaluation of the OCT-OA was performed using the cortical phantom (Fig. 3). It was observed that intralipid exhibited a lower optical attenuation ($4.5 \pm 0.6 \text{ mm}^{-1}$) than the silicon tube and titanium dioxide versa gel. The lumen of the silicon tube was visualized based on the geometric shape with a mean optical attenuation of $5.9 \pm 0.9 \text{ mm}^{-1}$, while the superficial region of the titanium dioxide phantom exhibited a mean optical attenuation of $6.2 \pm 1.5 \text{ mm}^{-1}$.

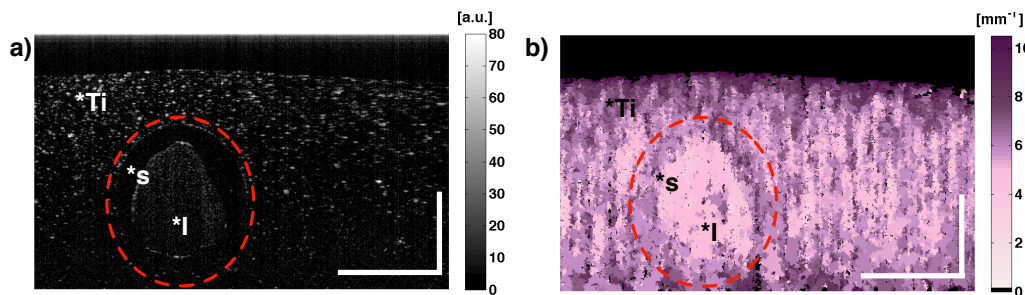


Fig. 3. (a) Structural OCT image of a cortical phantom which consisted of titanium dioxide versa gel (*Ti), silicon tube (*s) and diluted intralipid (*I). (b) The corresponding OCT-OA image of the cortical phantom. Scale bar: 1 mm.

3.2.2. Medulloblastoma imaging

To distinguish between normal brain ($N = 2$) tissue and medulloblastoma ($N = 3$), an alternative technique consisting of the estimation of optical attenuation coefficient from the OCT B-mode image was employed. The gross histology, the corresponding fluorescence image, and the combined image (gross + fluorescence) of the *Math1-GFP;Ptch^{+/−}* model can be seen in Fig. 4(a) to 4(c), respectively. Histological sections of normal cerebellum (Fig. 4(d)) were stained with hematoxylin and eosin (H&E). There are two major layers in the cerebellum: grey matter and white matter (*W). The grey matter consists of a molecular layer and a granular layer, which are separated by the Purkinje cell layer. These components were not visualized in the structural OCT image (Fig. 4(e)). Instead, the majority of the structural OCT image consisted of grey matter and appeared to be homogenous. In contrast, the OCT-OA image displayed a layered structure within the grey matter region (Fig. 4(f)). The color scheme in all OCT-OA images was selected to mimic H&E to help correlate the histology and OCT-OA. When correlating the OCT-OA image with the histology (Fig. 4(d)), the superficial layer of the OCT-OA image visualized the molecular layer with a mean optical attenuation of $4.8 \pm 0.6 \text{ mm}^{-1}$. Below this layer was the granular layer, which was depicted in the OCT-OA image as a “grainy region”. This grainy visualization may be related to the inherent hypercellularity in the granular layer relative to the molecular layer. From the histology, the right most lobe of the cerebellum contained granular layer that was superficial. This was also clearly seen in the OCT-OA image by its higher optical attenuation near the shallow regions of the tissue. The mean optical

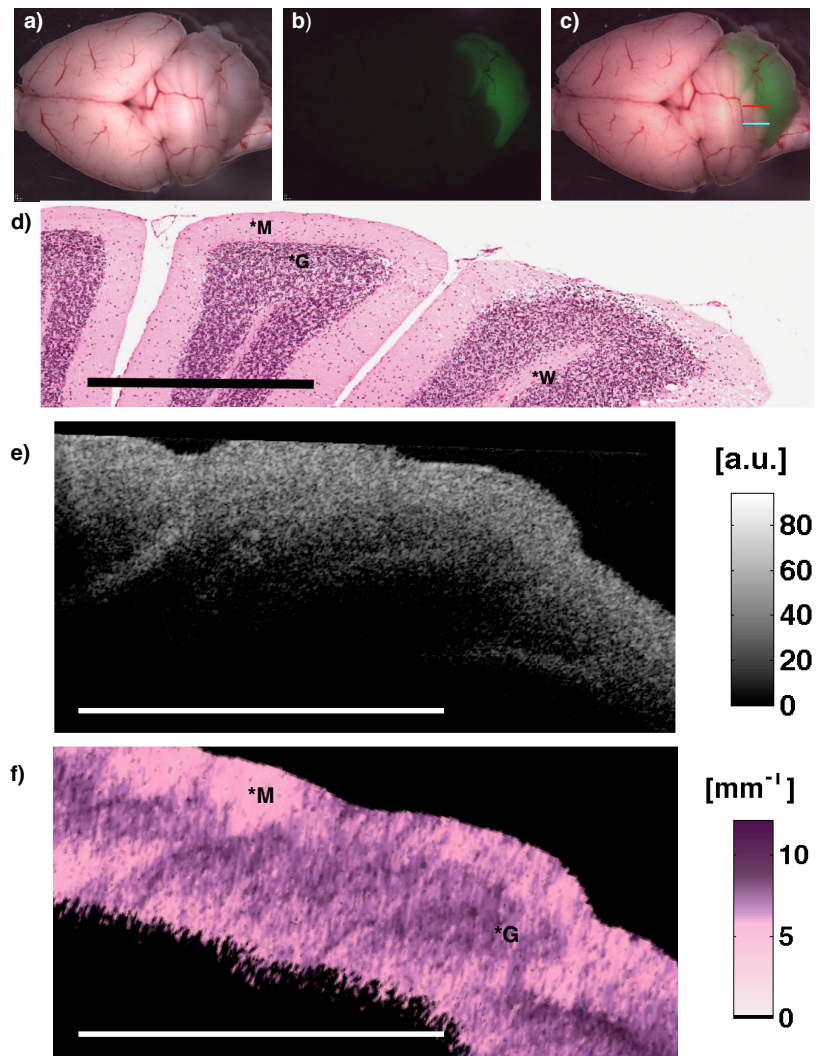


Fig. 4. (a) Gross histology of harvested *Math1-GFP;Ptch⁺⁻* mouse model. (b) The corresponding fluorescence image. (c) The combined gross and fluorescence image. Normal cerebellum (cyan line) and an interface of normal/medulloblastoma (red line) scans were taken. (d) H&E section of the cerebellum. Grey matter consisting of molecular layer (*M) and granular layer (*G) was observed. Underneath the granular layer, regions of white matter are present (*W). (e) The associated structural OCT with minimal resolved features. (f) The corresponding OCT-OA image consisted of a layered structure. The shape and location of these layers are similar to the molecular layer (*M) and granular layer (*G). Scale bar 500 μ m

attenuation of the granular layer was measured to be $7.1 \pm 0.3 \text{ mm}^{-1}$.

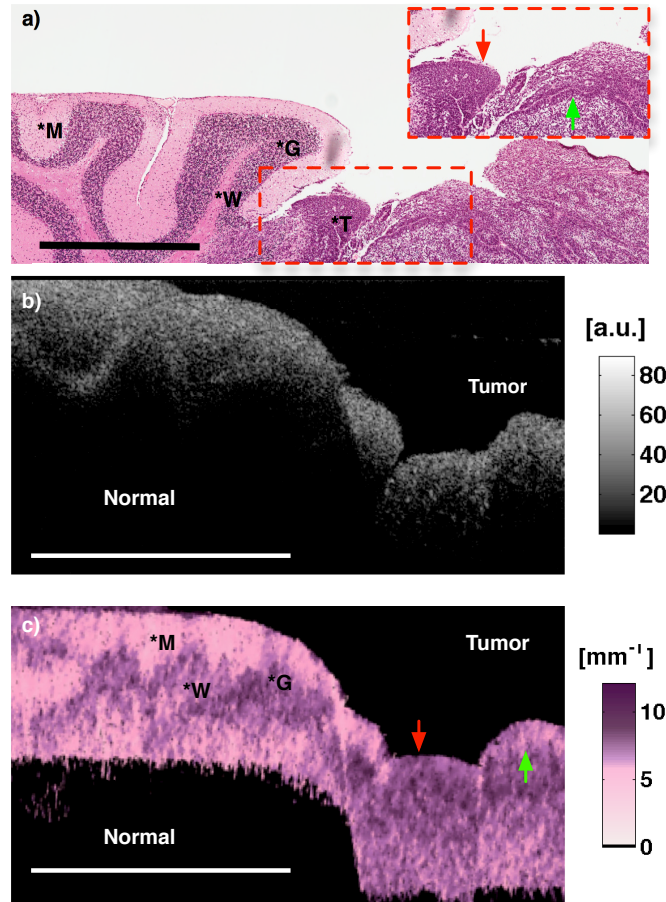


Fig. 5. (a) H&E section of the cerebellum in a *Math1-GFP;Ptc1^{+/−}* model. Grey matter consisting of molecular layer (*M) and granular layer (*G) was observed. Underneath the granular layer, regions of white matter (*W) are present. Regions of medulloblastoma resided on the right side (*T). Within the red dashed box, medulloblastoma regions that were adjacent to normal cerebellum demonstrated very dense cellular proliferation (red arrow). On the right side of the medulloblastoma region, superficial cells appear to be sparsely spaced (green arrow); however a lining of dense cells was located below. (b) The corresponding structural OCT with minimal resolved features. (c) The OCT-OA image consisted of a layered structure and erratic high attenuation region. In normal tissue the layers consisted of the molecular layer (*M) and granular layer (*G). The erratic high attenuation region was where medulloblastoma (*T). Scale bar 500 μm .

In a region where there was an interface between normal tissue and medulloblastoma (red line in Fig. 4(c)), a scan was performed with the OCT system (Fig. 5(b)). Histological sections revealed hypercellular regions that were associated with medulloblastoma lesions (*T) near the cerebellum. These individual tumor cells were small and contained hyperchromatic nuclei. Contralateral to the infiltrated hemisphere, the locations of both the normal tissue and medulloblastoma have a homogenous appearance in the structural OCT image (Fig. 5(b)). The delin-

eration between normal tissue and medulloblastoma was more notable in the OCT-OA imaging (Fig. 5(d)). The OCT-OA showed a lack of layered structures in medulloblastoma regions. Furthermore, these areas have higher attenuation coefficients (mean $7.8 \pm 0.4 \text{ mm}^{-1}$) compared to normal cerebellar tissue. The medulloblastoma region adjacent to normal cerebellar tissue exhibited dense cellularity (red arrow) compared to the posterior section of the tumor (green arrow). On the right side of image, a thin lining of dense cellularity resides beneath relatively sparse cells. Both the dense region and thin lining appeared to be leptomeningeal, whereas the regions above and below the thin lining of dense cells were non-neoplastic granule cells. The OCT-OA image (Fig. 5(c)) captured this feature as a lower optical attenuation coefficient near the surface. Normal cerebellum was also imaged and evaluated using the OCT-OA technique (Fig. 6). Similar to the previous specimen, the shape of the granular layer in the OCT-OA image (Fig. 6(c)) exhibited similarities with histology (Fig. 6(a)).

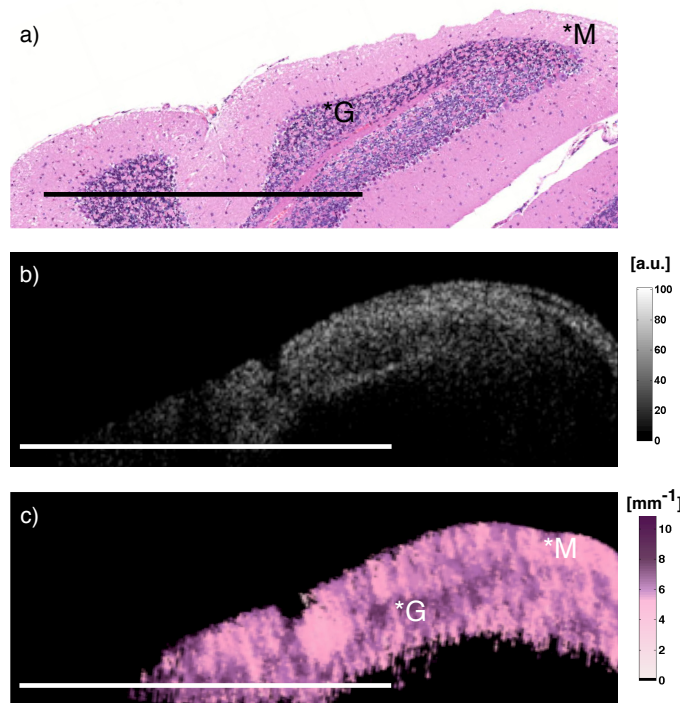


Fig. 6. (a) H&E section of a normal cerebellum where the molecular layer (*M) and granular layer (*G) are visualized . (b) The associated structural OCT image. (c) The corresponding OCT-OA image consisted of a high optical attenuation coefficient region (granular) and low optical attenuation (molecular). Scale bar 1 mm.

A surface prospective (transverse plane) structural 3D OCT image of the cerebellum with infiltrated medulloblastoma is displayed in Fig. 7(a). Boundaries between normal cerebellum (*C) and medulloblastoma (*T) were difficult to differentiate. In the corresponding OCT-OA image (Fig. 7(b)), infiltrated medulloblastoma regions were distinct. Higher attenuation coefficient regions are highlighted in dark purple, whereas normal cerebellum consisted of lower attenuation coefficient (pink regions). In both of the transverse images, a superficial blood vessel (white arrow) appeared to bridge between normal tissue and medulloblastoma regions. In the sagittal plane of the 3D OCT-OA image, 3 layers in normal cerebellum were visualized.

By magnifying the corresponding regions, the molecular layer (green arrow) and granular layer (black arrow) were ascertained. An additional layer resembling white matter on histology, was realized (red arrow) and had a mean optical attenuation coefficient of $5.2 \pm 0.4 \text{ mm}^{-1}$. The large purple region is an artefact due to the surface of the tissue being positioned beyond the zero path difference. A fly-through of the entire 3D OCT-OA demonstrated a consistent delineation between the different tissue types ([Media 1](#)). More specifically, the white matter was identified as a continuous layer enveloped by the granular layer. The overall mean and standard deviation of the aforementioned key morphological features of all the specimens are reported in Table 1. For each tissue type, the data points were averaged within individual mouse. T-test was performed and compared between the tissue types and all remaining tissues. It should be noted that two of the medulloblastoma models had significant infiltration of the cerebellum resulting in only medulloblastoma tissue.

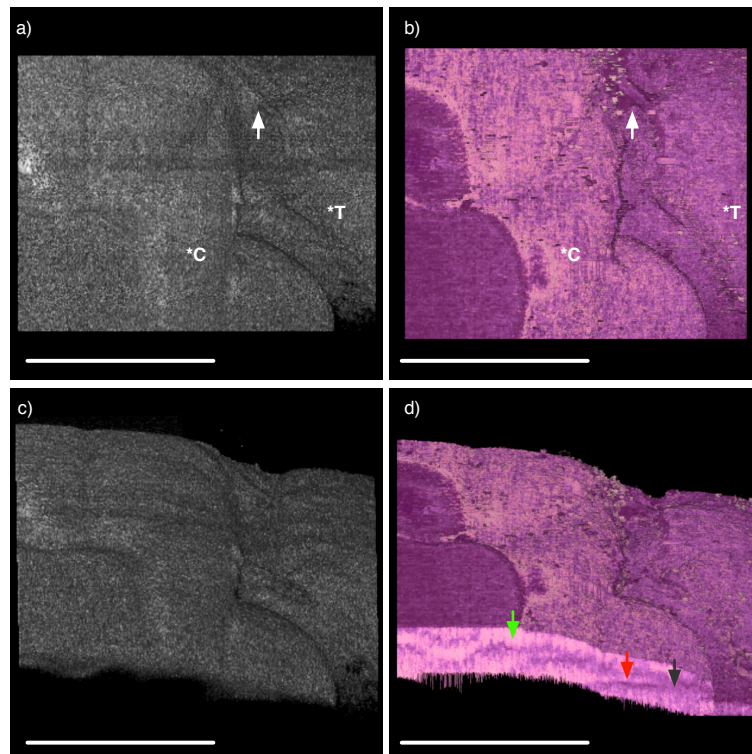


Fig. 7. (a) A surface prospective (transverse plane) from 3D reconstruction of structural OCT. Normal cerebellum (*C) and medulloblastoma (*T) regions were difficult to differentiate. (b) The same perspective was rendered from 3D OCT-OA images. Regions of normal cerebellum and medulloblastoma are clearly visualized. Both 3D OCT and 3D OCT-OA consisted of the visualization of a superficial blood vessel (white arrows). (c) Cross sectional regions in the 3D structural OCT image demonstrated few morphological features. (d) The corresponding 3D OCT-OA image exhibits layered structures. In the cross sectional regions, key morphological features were observed. The molecular layer (green arrow), granular layer (black arrow) and white matter (red arrow) could be resolved. A fly-through of the entire 3D OCT-OA is shown in [Media 1](#). Scale bar 1 mm.

Table 1. Summary of optical attenuation coefficient by tissue type

Tissue Type	μ_t (mm ⁻¹)	p-value
Molecular Layer (n= 3)	4.8 +/- 0.6	0.015
Granular Layer (n= 3)	7.1 +/- 0.3	0.078
White Matter (n= 3)	5.2 +/- 0.4	0.034
Medulloblastoma (n= 3)	7.8 +/- 0.4	0.002

4. Discussion

4.1. Refractive index

In this study, refractive index was one of the optical characteristics measured for medulloblastoma. The mean refractive index of normal brain specimen was lower than that of medulloblastoma, although given the standard deviation, the reported refractive index did not demonstrate a statistically significant difference. Nevertheless, the difference in the mean may be the result of the higher cellularity in medulloblastoma compared to normal tissue. These values appeared to be in the same order of magnitude to various anatomical regions in the mouse brain [24]. Furthermore, it has been reported that there was little differentiation in refractive index between the thalamus, cerebral cortex and the hippocampus [24].

The refractive index measurements were invasive in this study. Non-invasive measurements of refractive index would be more advantageous for *in vivo* measurements. Tearney *et al.* [25] demonstrated an alternative technique for the measurement of refractive index by tracking the focal position of the objective relative to the focus of the sample. This method would be suitable *in vivo* without sacrificing accuracy. Furthermore, *in vivo* refractive measurements were a rapid and simple method to distinguish the different tissue types. However, this measurement lacks the ability to visualize microstructural tissue layers required during surgical resection.

4.2. Optical coherence tomography optical attenuation imaging

The measurement of optical attenuation coefficient through OCT was also presented and compared with various corresponding morphological layers in the tissue. Regions that contained low to moderate cellularity, such as the molecular layer in the cerebellum had an optical attenuation coefficient range of 4 to 6 mm⁻¹. High cellularity in medulloblastoma had an average optical attenuation coefficient that was > 7.8 mm⁻¹. This may provide *in vivo* contrast for surgeons to detect margins. However, the optical attenuation coefficient values (Table 1) were not always the unique quantifier. The geometric shape and location of the OCT-OA image had to be accounted for in order to classify the tissue type. Layered structures seen in the OCT-OA image were inherently identified as normal tissue. The “inverse boot-like” shape of moderately cellular tissue was similar to the granular layer visualized through histology. Within the granular layer, a thin low attenuating segment denoted the white matter. As a result, a fairly accurate representation of OCT-OA imaging and histology was shown.

Overall, the OCT-OA measurements demonstrated good agreement with previously reported measurements of optical attenuation coefficients. In the vessel wall of a healthy coronary artery, the typical optical attenuation coefficient values were measured to be 2 to 5 mm⁻¹ at 1300 nm [17]. In terms of tumors, the optical attenuation of renal cell carcinoma was measured using a 1300 nm OCT system resulting in a median value of 8.85 mm⁻¹, while normal renal tissue had a median value of 4.95 mm⁻¹ [15]. Jeon *et al.* [31] had reported a higher optical attenuation

measurement within the grey matter of the hippocampus relative to white matter. It should be noted that the morphology of the granular layer in the hippocampus is different from the granular layer in cerebellum. This would result in a deviation between the previously reported values relative to white matter. The optical attenuation coefficient of white matter was reported to be $6.32 \pm 0.5 \text{ mm}^{-1}$, similar to the values reported in this work. Bevilacqua *et al.* [32] had previously shown higher optical attenuation measurements in medulloblastoma tissue compared to white matter. It should be noted evaluating the tissue at submicron NIR wavelengths and within an averaged volume of tissue would be different from the values reported in this work. Despite the similarities and differences between the previously reported optical attenuation measurements, further investigation is warranted.

There are several challenges that would arise during the translation of OCT-OA imaging to an *in vivo* mouse model and clinical OR environment. To achieve a calibrated OCT-OA image, a homogenous phantom was placed at the same elevation as the surface of the tissue. In both the *in vivo* mouse model and OR, the subject's physiological bulk motion would constantly change, which would potentially move beyond the set elevation measured using the phantom, resulting in an inaccurate OCT-OA measurements. Furthermore, the resection of tissue would lead to the presence of blood in the surgical and imaging field. The OCT signal would be significantly scattered, leading to the inability to resolve tissue structure due to shadowing. Constant arrogiation of the exposed region could reduce the effect of blood while reducing high surface reflections from the tissue.

4.3. Study limitation

The predominant limitation of this study revolved around OCT-OA imaging. As previously outlined by van Soest *et al.* [17], this method could not measure the backscattering coefficient resulting in artefacts and overestimates of optical attenuation coefficients at sharp interfaces between different tissues. Furthermore, the minimum size window that was used to evaluate the white matter would not be sufficient be in estimating the optical attenuation coefficient. It can be seen from the cortical phantom that clusters of highly reflective particles are believed to be titanium dioxide. In this case, the window size is significantly larger than the titanium particles, manifesting as a large standard deviation in the attenuation coefficient.

Among the previously reported limitations of OCT-OA [17], the addition of mean shift segmentation increased the computation time significantly. To achieve *in vivo* OCT-OA imaging, specialized hardware such as graphical processing units and parallel computing would be required. Optimization of the radius parameter would also need to be explored, as well as speckle reduction techniques to further improve OCT-OA imaging [19].

In terms of the refractive index measurements, the thin $500 \mu\text{m}$ slices would contain the granular layer. Based upon the reported similarities in the optical attenuation coefficient between the medulloblastoma tumor and granular layer, it is suggested that the refractive index of both these tissue types are also similar. In the human clinical environment, the molecular layer and granular layers are thicker. As a result, it is believed that the refractive index between normal human cerebellum and medulloblastoma would be significantly different. The increased specimen size would also provide a more accurate optical attenuation measurement as each tissue layer could be isolated. Additionally, a comprehensive analysis of the tumor can also be achieved at different depths.

Correlation between histology and OCT was a challenge in this study. During histological processing, the specimen would deform in shape and shrink, compared to the fresh state of the specimen during OCT imaging. The consequence of this deformation produced discrepancies between histology and OCT imaging.

5. Conclusion

In this study, refractive index and optical attenuation coefficient measurements of normal brain tissue and medulloblastoma in mouse models were achieved. Trends were also observed between the refractive index values, although statistically not significant. Furthermore, OCT-OA provided a more robust optical evaluation of brain tissue. Fundamental layers in grey matter and white matter were defined. This provided additional contrast to the boundary lines of medulloblastoma, which were difficult to delineate in the structural OCT image. The overall visualization of OCT-OA correlated well with histology and may have a potential for future exploitation in the clinical setting.

Acknowledgments

The authors acknowledge Adrian Mariampillai, Michael C. Kolios, Golnaz Farhat, Dimitri Androutsos, Jamil Jivraj, Helen Genis, Joel Ramjist, Ronnie Wong, Nicole Dinn, and Beau A. Standish for their technical assistance and helpful discussions. This work was supported by the Canadian Institutes of Health Research, the Natural Sciences and Engineering Research Council of Canada, the Ontario Brain Institute, Ryerson University, the Canada Research Chair Program, and the Canada Foundation for Innovation.